ROYAL SOCIETY
OF CHEMISTRY

EDGE ARTICLE

Check for updates

All publication charges for this article
have been paid for by the Royal Society
of Chemistry

Unraveling the origin of enhanced safety in capacitive-type carbon electrodes for 20C sodium-ion capacitors

Bo Xiong,[a] Jieming Cai,[a] Biao Zhong,[a] Luoming Zhang,[a] Dongxiao Li,[a] Jie Li,[a] Juan Tian,[b] Xiongwei Luo,[b] Fei Yao,[b] Zhiyu Zeng,[b] Wentao Deng,[a] Hongshuai Hou, [ID][a] Jialuo She,*[c] Tianyun Qiu,*[d] Guoqiang Zou, [ID]*[a] Dulin Yin[c] and Xiaobo Ji [ID][a]

Sodium-ion capacitors (SICs) combine battery-type and capacitive-type electrodes to achieve both high energy density and high power density. However, the capacity of conventional capacitive carbon materials is typically limited to below 120 mA h g^{-1}, resulting in inferior energy density for SICs. Therefore, the development of high-capacity capacitive electrode materials is considered critical. Herein, capacitive soft carbon (SC) is synthesized through *in situ* phosphorus crosslinking strategies applied to coal tar, with the resulting material exhibiting a high tap density of 1.26 g cm^{-3}, which is larger than that of other carbon materials (<0.81 g cm^{-3}). Furthermore, the obtained carbon materials deliver a high capacitive capacity of 308 mA h g^{-1} at 0.03 A g^{-1}. Impressively, *in situ* Raman characterization reveals that the P–O–C/P–C bonds introduced by *in situ* crosslinking can provide abundant reversible capacitive sodium storage sites, which effectively suppress Na–Na bonding, thereby inhibiting sodium dendrite formation and enhancing safety, according well with DFT calculations. When assembled into SICs, an ultrahigh energy density of 196.81 Wh kg^{-1} is achieved at 2891.90 W kg^{-1}, greatly surpassing previous reports (<120 Wh kg^{-1}). In a pouch cell (PC) configuration, a high energy density of 56.04 Wh kg^{-1} can be achieved at a high rate of 20C, with full charge accomplished within 96 seconds. This work provides essential guidance for constructing SICs with both ultrahigh energy and power densities.

Introduction

With the escalating fossil energy crisis, the contradictions between growing energy demands and depleting fossil fuel reserves are increasingly being highlighted.[1–6] Energy storage is recognized as a critical enabler for large-scale renewable energy grid integration, advancement of new energy vehicles, and achievement of carbon peak and carbon neutrality goals.[7] Consequently, next-generation large-scale energy storage devices integrating high energy and power densities are urgently required for electric vehicles and smart grid applications.[8] Sodium-ion capacitors (SICs) are positioned to potentially combine the high power capability of traditional electrochemical capacitors with the high energy density advantages of batteries.[9] The development of high-rate anode materials featuring low cost, high capacity, and long-term cyclability represents a pivotal challenge for advancing SICs. Carbon-based materials are regarded as promising candidates for practical SICs due to their highly stable structures and cycling durability.[10] Among various carbonaceous anodes for SICs, hard carbons (HCs) have garnered significant attention in recent years owing to their economic advantages, wide availability, and optimal overall performance.[11] However, the suboptimal initial coulombic efficiencies (ICEs) and poor rate capabilities of HCs remain primary bottlenecks that hinder future commercial deployment.[12]

Until now, various precursors have been used in an attempt to overcome the above obstacles. For example, multiple structural features in HC were accurately constructed by Wu *et al.* through the sulfuric acid treatment of bamboo powder, where the precursor composition was adjusted, resulting in RHC with an excellent rate capability (108.8 mA h g^{-1} at 8 A g^{-1}).[12] Bituminous coal was acid-washed by Wang *et al.* using a molten-salt-assisted method to adjust the HC microstructure, achieving a rate capability of 82.1 mA h g^{-1} at 500 mA g^{-1}.[13] Soft carbon (SC) with a rate capability of 155 mA h g^{-1} at 1.5 A g^{-1} was synthesized at low temperature by Qi *et al.* utilizing

^{a}College of Chemistry and Chemical Engineering, Central South University, Changsha, 410083, Hunan, China. E-mail: gq-zou@csu.edu.cn

^{b}Hunan Changlian New Material Technology Co., Ltd., China

^{c}National & Local United Engineering Laboratory for New Petrochemical Materials & Fine Utilization of Resources, College of Chemistry and Chemical Engineering, Hunan Normal University, China. E-mail: dingbang53191@163.com

^{d}School of Photovoltaic and Renewable Energy Engineering, UNSW Sydney, Australia. E-mail: tianyun.qiu@unsw.edu.au

bitumen.[14] Nevertheless, there are many issues to consider for large-scale production from the above strategies, and practical applications need to consider microstructure modulation based on high prices and complex processes.[15] Inexpensive coal tar is a remarkable choice for large-scale production, and so far no in-depth studies have been carried out on improving the performance of coal-derived carbon materials with high tap density and high rate capability.

By comparing with other studies,[16] it is not difficult to find that the capacity and ICE of coal-derived carbon materials are low, but recent articles, as shown in Table S1, mainly focus on improving the capacity at low current densities, and tend to neglect the rate capability at high current densities. The poor rate capability cannot satisfy the scenarios of the existing new energy vehicles that are rapidly fully charged, which greatly limits the commercialization. As such, the commercialization of coal-derived carbon materials urgently requires that the rate capability be enhanced while ensuring safety to meet fast-charging/discharging demands, with high capacity and tap density simultaneously maintained to elevate the volumetric energy density.

This paper reports the synthesis of capacitive SC through *in situ* phosphorus crosslinking strategies applied to coal tar, with the resulting material exhibiting a high tap density of 1.26 g cm^{-3}, which is larger than that of other carbon materials (0.81 g cm^{-3}). The coal-tar-derived carbon produced *via* this approach was demonstrated to achieve an 80% yield while maintaining low raw material costs. Furthermore, the obtained carbon materials deliver a high capacitive capacity of 308 mA h g^{-1} at 0.03 A g^{-1}. Impressively, *in situ* Raman characterization reveals that the P–O–C/P–C bonds introduced by *in situ* crosslinking can provide abundant reversible capacitive sodium storage sites, which effectively suppress Na–Na bonding, thereby inhibiting sodium dendrite formation and enhancing safety, according well with DFT calculations. This configuration was found to contribute $277.7 \text{ mA h g}^{-1}$ capacity in the slope region (>0.1 V *vs.* Na/Na$^+$), enabling the realization of both ultrahigh energy density ($196.81 \text{ Wh kg}^{-1}$) and ultrafast charge/discharge capabilities on a seconds-level timescale. More significantly, when sodium iron pyrophosphate phosphate (NFPP) is employed as the cathode, high safety, superior rate capability, and ultrahigh energy density are integrated in both button SICs and pouch cells (PCs). This straightforward and scalable methodology could offer the possibility of developing practical SICs exhibiting both high power density and high energy density.

Results and discussion

Theoretical calculations

Firstly, three distinct structural models were established: pristine monolayer graphene (MC), phosphorus-doped graphene featuring P–C bonds (MPC) and phosphorus-doped graphene featuring P–O–C bonds (MPOC). By means of Density Functional Theory (DFT) calculations, the influence of adsorbing varying numbers of Na$^+$ ions on the sodium-ion adsorption energy (E_{ad}) for each model was systematically investigated

(Fig. 1a–c). Numerically, all three models exhibited a consistent trend: the E_{ad} value became more negative as the number of adsorbed sodium ions increased (Fig. S1). Furthermore, taking the adsorption of two sodium ions as a specific example, the E_{ad} value was more negative when interactions existed between the adsorbed sodium ions compared to the scenario without such interactions (Fig. S2). This observation suggests that, during sodium storage within the slope voltage region, Na$^+$ ions exhibit a tendency to interact with each other. Consequently, the voltage decrease observed in the slope region during the charging of sodium-ion batteries (SIBs) may be attributed to the gradual increase in the number of Na$^+$ ions adsorbed and stored within the anode material. Comparing MPC with MPOC, MPOC exhibited a stronger adsorption energy than MPC. It is indicated that the P–O–C bonds offer superior sodium storage capability and enhanced dendrite suppression compared to the P–C bonds, consequently leading to improved rate capability.

Considering that the E_{ad} value of a single sodium ion is measured as -1.42 eV (Fig. S3), all E_{ad} values in MC are found to be greater than -1.42 eV. It is indicated that sodium metal exhibits a stronger adsorption affinity toward sodium ions than that of MC, which provides an explanation for the formation mechanism of sodium dendrites. In contrast, the E_{ad} values for both MPC and MPOC with 3–4 adsorbed sodium ions are determined to be less than -1.42 eV. It is demonstrated that phosphorus-doped graphene can enhance the adsorption capability of carbon toward sodium, thereby suppressing the adsorption between Na$^+$ ions. Secondly, the Electron Localization Function (ELF) was calculated for the three models (Fig. 1d). The degree of electron localization in space is visualized *via* the ELF. By comparing the electron distribution across the three models, it is revealed that the electrons contributed by the P atom are uniformly distributed across the graphene plane in MPC. In contrast, electrons are contributed by both P and O atoms in MPOC. Subsequently, the Charge Density Difference (CDD) was computed for the three models (Fig. 1e). In these models, an increase in electron density is indicated by yellow regions, while a decrease is indicated by blue regions. Electron transfer from the graphene plane to the adsorbed Na$^+$ ions is observed. Notably, electrons are donated by O atoms to both Na and P atoms in MPOC. Compared to electron donation solely from P atoms in MPC and C atoms in MC, a stronger electron-donating capacity is exhibited by MPOC. It is revealed that the enhanced sodium storage capability is facilitated by the presence of the P–O–C bonds. Compared to the model adsorbing four sodium ions, E_{ad} values of -0.85 eV, -2.92 eV, and -2.41 eV were calculated for MC (Fig. 1a4), MPC (Fig. 1b4), and MPOC (Fig. 1c4), respectively. This demonstrates that lone-pair electrons are provided by P/O doping, modifying the electron distribution of graphene and enhancing the sodium adsorption strength. Through electronic structure modification, uniform nucleation is enabled while initial dendrite nucleus formation is suppressed.

Finally, the Partial Density of States (PDOS) was calculated for the three models (Fig. 1f). A larger magnitude of density of states in the vicinity of the Fermi level (E_{F}) is exhibited by MPOC compared to the other two models, signifying superior electrical
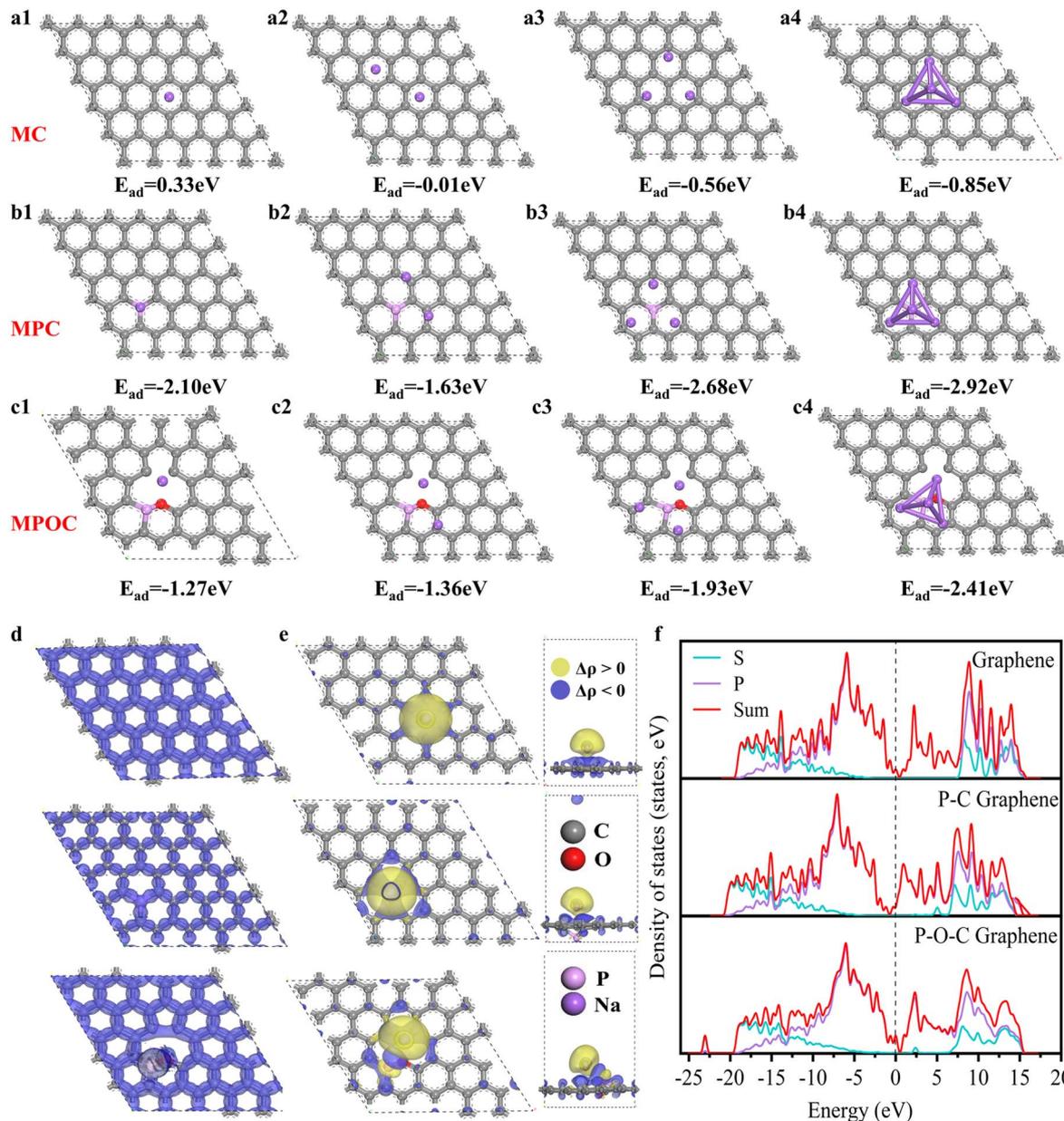
Fig. 1 (a1–a4) E_{ad} on MC with varying numbers of Na$^+$ ions; (b1–b4) E_{ad} on MPC with varying numbers of Na$^+$ ions; (c1–c4) E_{ad} on MPOC with varying numbers of Na$^+$ ions; (d) the ELF images of the three models; (e) the CDD images of the three models; (f) the PDOS images of the three models.

conductivity. Moreover, within the energy range of −3 eV to 3 eV, a larger density of states area is possessed by MPOC compared to MC, indicating a greater number of active sites.

Structural characterization

The typical preparation process for PCT-800 is shown in Fig. S4, where low-temperature crosslinking, intermediate-temperature sintering and secondary annealing treatments were performed sequentially.

The phase structure of the material was investigated by X-ray diffraction (XRD) analysis. As illustrated in Fig. 2a, two broad diffraction peaks are observed at approximately 25° and 43.8°,

which are attributed to the (002) and (100) crystallographic planes of a disordered amorphous structure, respectively. As the temperature is increased from 800 °C to 1200 °C, a continuous shift of the amorphous carbon (002) peak toward higher angles is observed. This shift is attributed to progressive enhancement of local graphitization within the SC structure. Concurrently, progressive sharpening of the peak is detected, which is indicative of increased crystallite size and reduced defect concentration. The layer spacing (d_{002}) of the amorphous carbon (002) peaks, as well as the average grain width (L_a) and grain height (L_c) of the graphite microcrystals, are further calculated using the Bragg's equation and Scheller's formula, as shown in Table S2, Fig. S5 and S6.
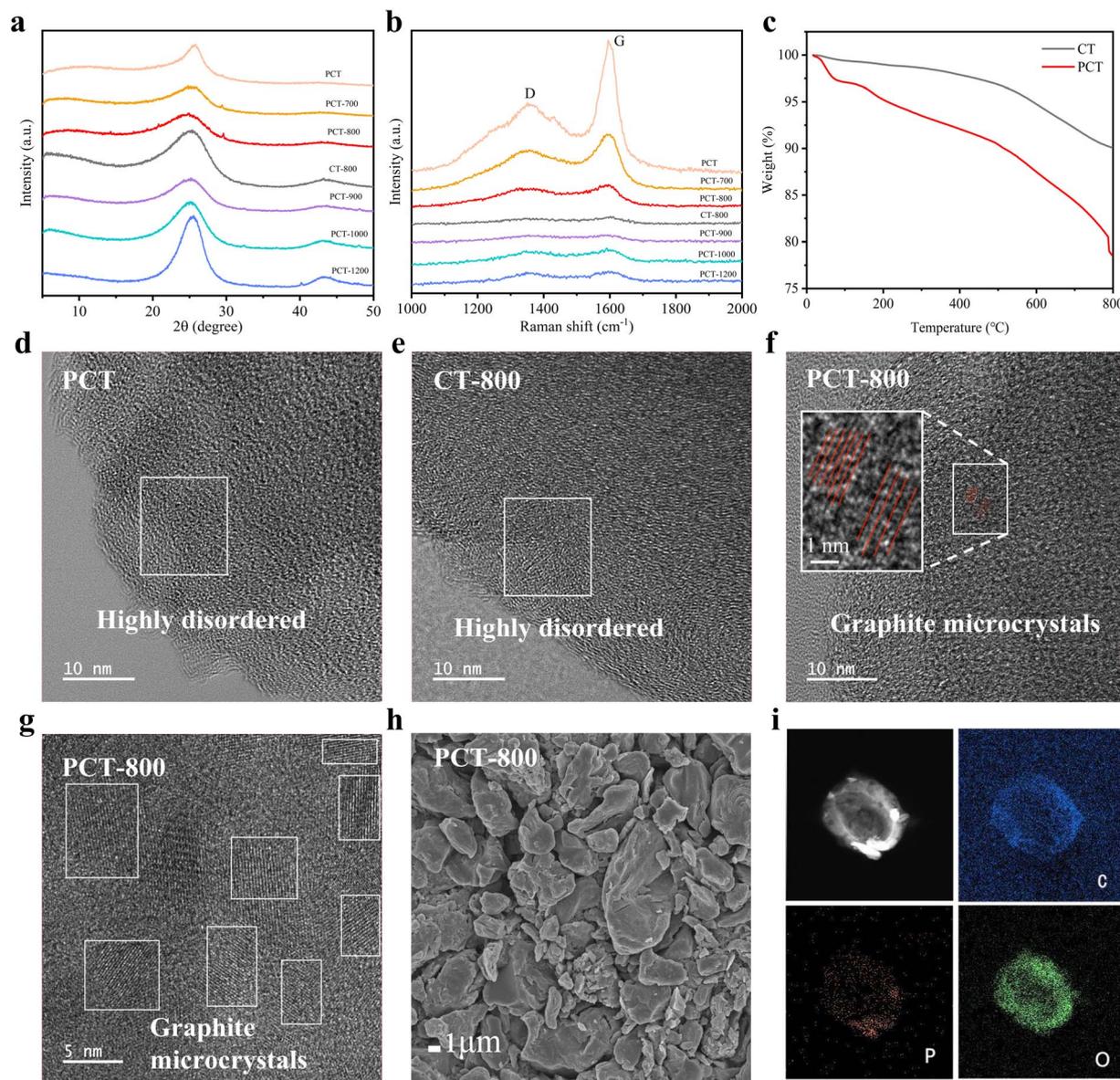
Fig. 2 (a) XRD pattern of PCT-*X* samples; (b) Raman spectra of PCT-*X* samples; (c) TG analysis of PCT and CT samples; (d–f) TEM images of PCT, CT-800, and PCT-800 samples near the surface; (g) graphite microcrystalline regions of PCT-800 samples in the bulk phase; (h) SEM image of PCT-800; (i) EDS elemental mapping images of PCT-800 samples.

As the temperature is elevated from 800 °C to 1200 °C, a reduction in the d_{002} spacing of amorphous carbon from 0.36 nm to 0.35 nm is observed, strongly confirming the enhancement of local graphitization. Concurrently, increases in both L_a and L_c are detected over the same temperature range. This trend is interpreted as indicative of progressive enlargement of graphitic crystallite dimensions at higher temperatures. These results, in combination with the electrochemical performance data (Fig. 4a), which reveal gradual capacity fading, demonstrate that sodium storage is optimally achieved in the microstructures with appropriate dimensions. Specifically, superior performance is attained when graphitic crystallites are stabilized in a short-range ordered configuration characterized by a reduced number of stacking layers.

The comparison of PCT-800 (0.36 nm) and CT-800 (0.35 nm) shows that phosphorus doping helps to expand the layer spacing.[17] The crosslinker is utilized to interweave asphalt molecular units, transforming linear molecules into three-dimensional porous polymers.[18] During carbonization, this strategy is shown to effectively suppress disordered stacking of the carbon layers while enhancing material compaction performance. The tightly stacked graphite microcrystals resulted in a higher tap density (1.26 g cm^{-3}), as shown in Table S3. As shown in Fig. S7, a larger interlayer spacing of 0.39 nm is measured for commercial hard carbon (CHC). This structural characteristic is correlated with a lower tap density of 0.81 g cm^{-3}.

To further explain the changes in the defects and carbon structure of the samples, Raman spectroscopy was employed (Fig. 2b). The D-band ($\sim$1350 cm^{-1}) and G-band ($\sim$1580 cm^{-1}) are identified as characteristic Raman peaks of carbon materials (*e.g.*, graphene, carbon nanotubes, and amorphous carbon). The D-band ($\sim$1350 cm^{-1}) is attributed to defect-induced phonon scattering caused by phosphorus doping, which generated disordered structures that included sp^3 hybridization, edges, vacancies, and dopant sites. The G-band shift ($\sim$1600 cm^{-1}) is influenced by phosphorus doping through two mechanisms: the Fermi level is modified (shifted toward higher energies) and a band gap is opened. Microstructural parameters for the soft carbon series are comprehensively summarized in Table S4. It can be observed that the value of I_D/I_G decreases sequentially from 2.514 to 1.087 as the carbonization temperature increases from 700 °C to 1200 °C (Fig. S8), indicating that the defect content decreases with increasing temperature, which leads to a decrease in capacity.

In order to explore the mass change during pyrolysis, thermogravimetric (TG) tests were performed (Fig. 2c). The curves decrease more steeply between 500 °C and 800 °C, suggesting that the decomposition or reaction of the sample is more intense in this temperature range, which results in a rapid weight loss. The lower PCT-800 carbon yield (80%) compared to the CT-800 carbon yield (90%) is due to the loss of P and reduction of defects during pyrolysis.[19] The superior carbon yield of PCT-800 (80%) compared to biomass-derived carbons ($\sim$20%) is enabled by the crosslinker, whose network formation was proven to effectively suppress pyrolytic volatile release, thereby elevating the final material yield.

The morphology and microstructure of the PCT, CT-800, and PCT-*X* samples (Fig. 2d–f and S9) were analyzed by transmission electron microscopy (TEM). Obviously, the PCT-800 sample is more visibly ordered than PCT and CT-800, and graphite microcrystals have appeared in the edge region, which is more distinct in Fig. 2g, where a large number of short-range-ordered and long-range-disordered graphite microcrystals are stacked together in the bulk phase. Moreover, graphite microcrystals exhibiting short-range-ordered, few-layer structures have been demonstrated to enhance sodium storage performance. The surface of the PCT-800 sample was further examined using scanning electron microscopy (SEM) and observed to have a lamellar structure (Fig. 2h), which echoes the planar structure of the tightly stacked graphite microcrystals. Meanwhile, energy dispersive spectroscopy (EDS) mapping revealed a uniform distribution of C, P, and O elements in the same thickness region of the PCT-800 sample (Fig. 2i).

In order to investigate the effect of different temperatures on the surface area and pore structure of the samples, N$_2$ adsorption–desorption tests were carried out. The N$_2$ adsorption–desorption isotherm of PCT-*X* (Fig. 3a) shows a type III isotherm, which indicates the presence of abundant mesopores (2–50 nm). The BET specific surface area (S_{BET}) increased and then decreased as the carbonization temperature increased from 700 °C to 1000 °C. The S_{BET} value (8.77 m^2 g^{-1}) of the PCT-800 material is the maximum value (Fig. S8). The S_{BET} values of the PCT-*X* materials are all less than 10 m^2 g^{-1}. This is due to

the fact that the diffusion and volatilization of small molecules inside the materials are inhibited, and it is difficult to form pores as freely as at atmospheric pressure, resulting in a relatively small number of pores inside the materials, along with the decrease of specific surface area accordingly. The lower the specific surface area, the higher the ICE.[20] A reduced S_{BET} (<10 m^2 g^{-1}) effectively suppresses electrolyte decomposition and sodium metal plating for SICs.[20] The pore size distribution diagram of BJH (Fig. 3b) shows that the pore size of PCT-*X* is mainly distributed in the range of 2–12 nm, which coincides with the type III isotherm.

Meanwhile, the Fourier transform infrared (FTIR) spectra (Fig. 3c) showed that the peaks of PCT and PCT-800 at 737, 1060, 1150 and 980/2380 cm^{-1} are attributed to the P–C, P–O–C, P=O and P–H bonds, respectively, which proves that the coal tar doped with phosphorus forms the phosphorus-containing chemical bonds in the PCT and PCT-800 materials. While CT-800 has no peaks in these three places, which is consistent with the fact that the CT-800 material is undoped coal tar with phosphorus. The peaks at 1350, 1710, and 3430 cm^{-1} are attributed to C–O, C=O, and O–H bonds, respectively, indicating that all three materials contained O atom, and C=O decreased after carbonization at 800 °C, which means that the oxygen content decreases along with temperature increasing. The peaks at 1580 and 1630 cm^{-1} are attributed to C–C and C=C bonds, respectively, and the peaks are stronger after carbonization at 800 °C, indicating that the carbon content increases with the increase of temperature. From PCT to PCT-800, the peaks of the P=O and P–H bonds are weakened or have disappeared, while the peaks of P–O–C are enhanced, indicating that the chemical state of the P species was transformed after annealing, which is in agreement with the subsequent analysis results.

The chemical composition and elemental states of the obtained materials were investigated by X-ray photoelectron spectroscopy (XPS) measurements. The PCT-*X* samples were all composed of three elements: C, P, and O (Fig. S10 and Table S4). As the carbonization temperature increased from 700 °C to 1200 °C, the C content increased, the O content gradually decreased, and the P content first increased and then decreased (Fig. S11). Specifically, for the C 1s fitted spectra of the PCT-*X* sample (Fig. 3d), the five main peaks located at about 283.8 eV, 284.8 eV, 286.0 eV, 287.4 eV, and 288.8 eV can be attributed to the C–P, C–C/C=C, C–O, C=O, and O–C=O functional groups, respectively. For the O 1s fitted spectra of the PCT-*X* sample (Fig. 3e), the three main peaks located at about 531.8 eV, 532.8 eV and 533.9 eV can be attributed to the C=O/P=O, C–O, and P–O–C functional groups, respectively. For the P 2p fitted spectra of the PCT-*X* sample (Fig. 3f), the four main peaks at about 129.5 eV, 130.5 eV, 132.7 eV and 134.7 eV can be attributed to the P–P, P–C, P–O and P=O functional groups, respectively. It is not difficult to find that P=O bonds are predominantly present in the precursor PCT, whereas P–O bonds become dominant in PCT-*X* samples after annealing. The percentage contents of C=O, C–P, and P=O in the PCT-800 samples are higher than those of the other PCT-*X* samples,
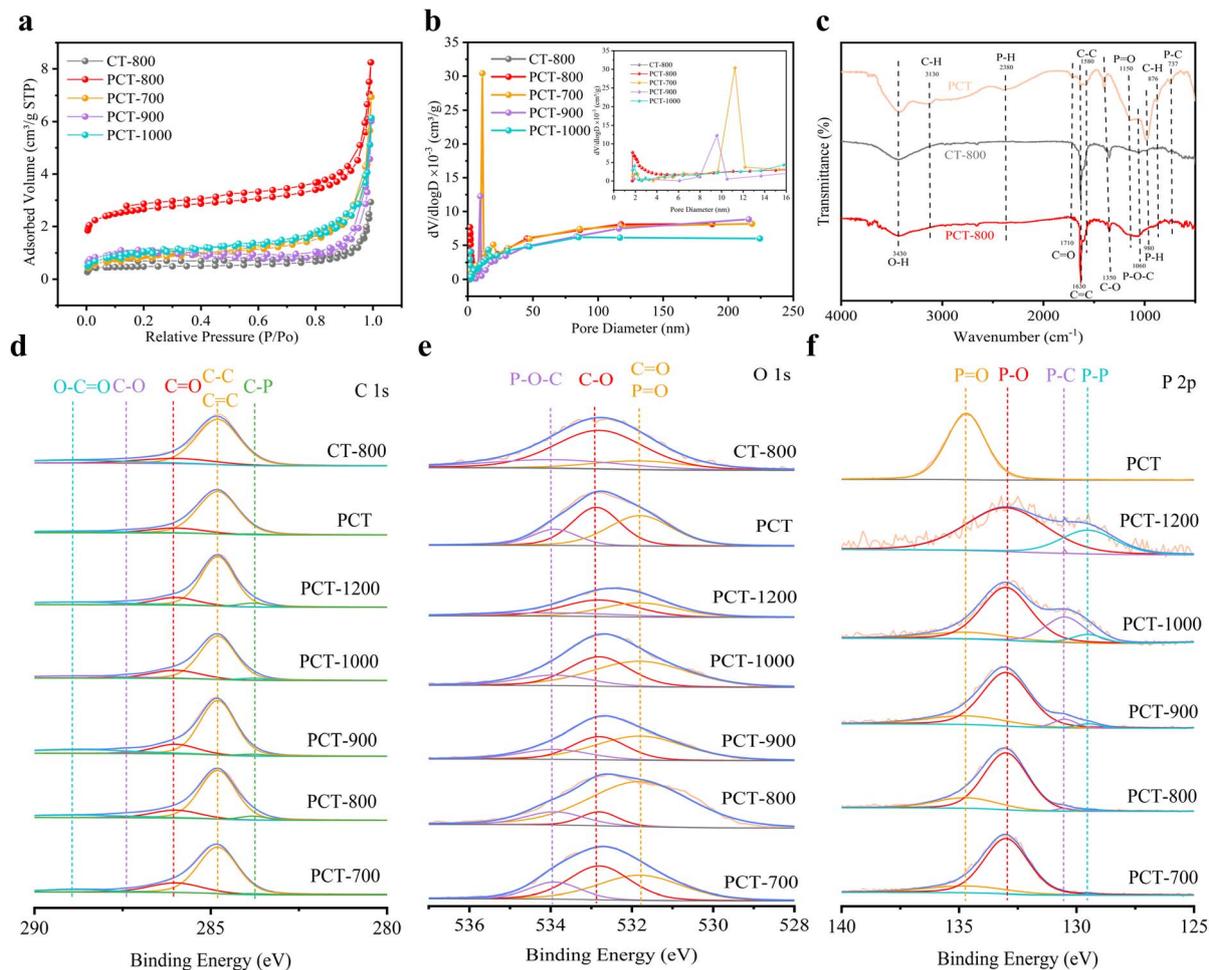
Fig. 3 (a) N_2 adsorption−desorption isotherm Raman spectra; (b) pore size distributions; (c) FT-IR spectra of the PCT-X samples; (d–f) C 1s, O 1s, and P 2p spectra of XPS of the PCT-X samples.

which favors the reversible adsorption of Na during electrochemical processes.[21]

Sodium storage performance of a half-cell device

In order to evaluate the electrochemical performance of the prepared SCs, constant current charge/discharge measurements were performed in an ether-based electrolyte (Fig. 4a–d). According to the Galvanostatic Charge–Discharge (GCD) curves (Fig. 4a), the obtained carbon materials deliver a high capacitive capacity of 308 mA h g^{-1} at 0.03 A g^{-1}. The capacity is mainly contributed by the slope capacity, and the plateau region below 0.1 V with a plateau capacity of less than 50 mA h g^{-1} is not obvious (Fig. S12). PCT-800 was demonstrated to deliver the superior slope capacity (277.7 mA h g^{-1}), whereas PCT-900 was found to exhibit the maximum plateau capacity (41.9 mA h g^{-1}). And the rate capability of PCT-900 (Fig. 4b) was superior at small current densities (0.05–1 A g^{-1}), which is consistent with the results in Table S4, where the P content of PCT-900 (3.77%) is slightly higher than that of PCT-800 (3.24%). It is noteworthy that the rate capability of PCT-800 (181 mA h g^{-1}) is superior to that of PCT-900 (168 mA h g^{-1}) at a high current density of 2 A g^{-1}, indicating that the sodium storage kinetics of PCT-800

are superior to those of PCT-900, which is consistent with the results in Fig. 2i for PCT-800 with the highest percentage of C=O content.

To explore the optimal specific capacity performance in the PCT-X samples, PCT-850 and PCT-950 were synthesized and tested (Fig. S13). Surprisingly, the maximum and minimum specific capacities at current densities of 0.1 A g^{-1} and 2 A g^{-1} are still not harmonized. Instead, the consensus is that the specific capacities of the PCT-X samples are much higher than that of CHC at current densities of 0.5, 1, and 2 A g^{-1}, which implies a better prospect for commercialization. The superior cycling performance of PCT-900 (Fig. 4c) is demonstrated by the fact that not only does it have the highest reversible capacity (264.5 mA h g^{-1}) at a current density of 0.1 A g^{-1}, but also higher capacity retention after 500 cycles (94.65%) compared with PCT-800 (89.17%). Comparing the cycling performance at high current densities (5 A g^{-1}), the reversible capacity of PCT-900 is still better than that of PCT-800 (Fig. S14). Considering commercialization, the rate capability of CHC and PCT-800 is compared based on volumetric specific capacity (Fig. 4d). At a current density of 0.1 A g^{-1}, the volumetric specific capacity of PCT-800 (307 mA h cm^{-3}) is found to significantly exceed that of
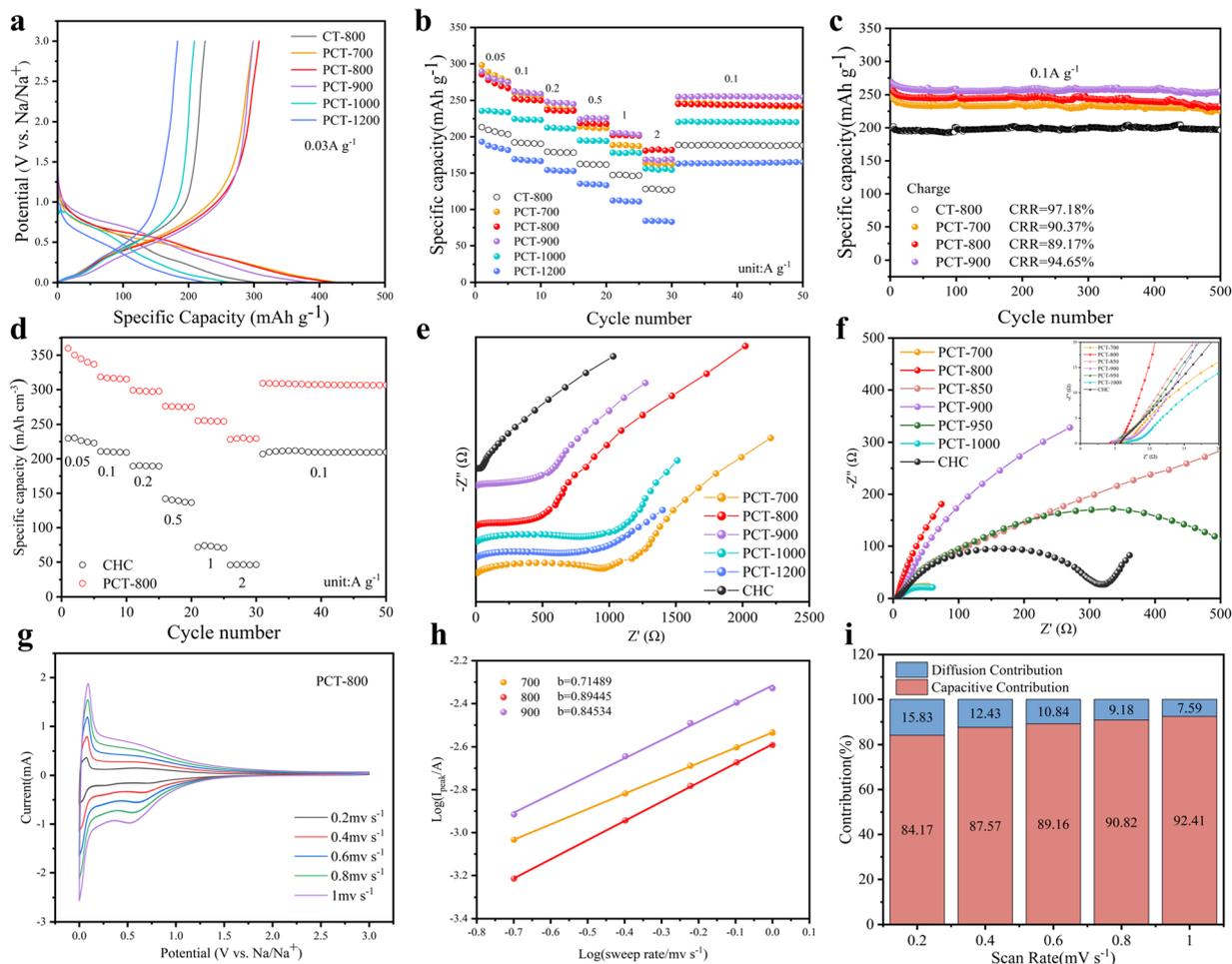
Fig. 4 (a) Comparison of the first charge/discharge curves; (b) comparison of the rate performance; (c) cycling behavior; (d) comparison of the rate performance based on the volumetric specific capacity; (e and f) EIS curves of the PCT series samples before and after cyclic testing; (g) CV curves of the PCT-800 anode; (h) the *b*-value of the PCT-*X* anodes; (i) contribution of diffusion and surface control of the PCT-800 anode at different scan rates.

CHC (209 mA h cm^{-3}). Notably, a substantial difference of 180 mA h cm^{-3} is observed at a high current density of 2 A g^{-1}.

The electrochemical behavior of the prepared soft carbon Na storage processes was further analyzed using electrochemical impedance spectroscopy (EIS) tests, especially for the study of interfacial charge transfer kinetics. The Nyquist diagram in Fig. 4e shows all the curves as a straight line and a semicircular arc, indicating that the PCT-*X* samples have similar electrochemical processes. Both before and after the cyclic testing, among all the PCT-*X* samples, PCT-800 and PCT-900 have the smallest charge transfer resistance along with diffusion impedance. Although the interfacial impedance of the CHC was smaller before the testing, the PCT-*X* samples had smaller interfacial impedance and faster sodium storage kinetics after the testing (Fig. 4f), which also coincided with the characterization of the rate capability (Fig. S15).

Cyclic voltammetry (CV) measurements were performed to investigate the kinetic properties of the sodium storage process. The CV curves of the prepared PCT-*X* samples were recorded at different scan rates ranging from 0.2 to 1.0 mV s^{-1}, and the curves all showed similar behavior (Fig. S16 and S17). A pair of distinct reversible redox peaks near 0–0.1 V, attributed to the adsorption and desorption of sodium ions, indicated the formation of a good solid electrolyte interface (SEI) layer at the PCT-800 electrode/electrolyte interface. A pair of broad peaks of weaker intensity near 0.55 V is attributed to the reversible electron transfer reaction of oxygen-containing functional groups (such as carbonyl groups) during the electrochemical process. According to the Randles–Sevcik equation (25 °C):

$$i_{\mathrm{p}} = (2.69 \times 10^5)n^{3/2}AD^{1/2}v^{1/2}c, \qquad (1)$$

where i_{P} is the peak current, n is the number of electrons transferred in the reaction, A is the electrode area, D is the diffusion coefficient, C is the reactant concentration, and v is the scan rate. Comparing the CV curve of PCT-*X* at 0.2 mV s^{-1} (Fig. 4g), the peak shape of PCT-900 is the sharpest and the peak current is the largest, which indicates that the charge transfer rate of PCT-900 is higher and the reaction kinetics are faster.

The contributions of the capacitance-controlled and diffusion-controlled processes are analyzed simultaneously. The relationship between peak current (i) and scan rate (ν) is established using the following equation:

$$i = a\nu^b, \tag{2}$$

where i is the peak current, ν is the scan rate, and a and b are constants. In particular, if b is close to 0.5, it indicates a diffusion-controlled encapsulation process, such as pore filling, while if b is close to 1, it corresponds to a surface-controlled capacitive process, such as adsorption. Here, the b value represents the slope of the $\log(i)$ versus $\log(\nu)$ curve. The b value of 0.89 for PCT-800 indicates that the kinetic behavior is dominated by capacitance-controlled processes (Fig. 4h), and the b value is higher than that of PCT-700 (0.71) and PCT-900 (0.85), suggesting that the rate capability of PCT-800 is superior at high current densities. Furthermore, the b values of the PCT-X samples are all observed to be close to 1, which implies that their sodium storage mechanisms in the slope region are principally governed by pseudocapacitive adsorption mechanisms.

To further quantify the contribution of diffusion-controlled and surface-controlled behaviors, the CV curves of the PCT-800 sample were further analyzed using the following equation:

$$i(\nu) = k_1\nu + k_2\nu^{1/2}, \tag{3}$$

where ν is the scan rate, and $k_1\nu$ and $k_2\nu^{1/2}$ represent the contributions of the surface-controlled capacitance and diffusion-controlled processes, respectively. As shown in Fig. 4i, the capacitance contribution ratios of the total capacity of the PCT-800 sample were calculated for different scan rates. The percentage of pseudocapacitive contribution increases with scan rate from 84.17% at 0.2 mV s^{-1} to 92.41% at 1.0 mV s^{-1}. Capacitive processes are crucial for electrochemical storage, especially for rate capability at high current densities. The pseudocapacitance contribution of more than 80% for PCT-800 is associated with ultra-fast sodium storage kinetics and excellent rate performance.

Analysis of the sodium storage mechanism

For the purpose of further confirming the structural changes and Na storage mechanism of the PCT-800 samples, in situ XRD, in situ Raman, ex situ XRD and ex situ XPS analyses were employed. The evolution of the functional groups in PCT-800 during the charging process was revealed through ex situ XPS analysis (Fig. 5a–c). For the C 1s fitted spectra (Fig. 5a), the five dominant peaks located at approximately 283.8 eV, 284.8 eV, 286.4 eV, 288.3 eV, and 289.1 eV are attributed to the C–P, C–C/C=C, C=O, C–O functional groups, and Na$_2$CO$_3$, respectively. In the O 1s fitted spectra (Fig. 5b), the three dominant peaks observed at approximately 531.2 eV, 532.8 eV, and 535.8 eV are separately assigned to the C=O, P–O functional groups, and (CF$_3$CH$_3$O)$_3$CO, respectively. Regarding the P 2p fitted spectra (Fig. 5c), the two dominant peaks positioned at approximately 132.9 eV and 137.2 eV are attributed to the P–O functional

groups and NaPF$_6$, respectively. From 0 to 3 V, Na$^+$ ions were gradually detached from the PCT-800 anode. In addition, the content of the C=O and C–P functional groups in the C 1s spectra, as well as the content of P–O in the O 1s spectra, gradually increased, and it is implied that the C=O, P–C, and P–O bonds were the sodium storage active sites. From 1 to 0.5 V during the discharge process, the decrease in the contents of the C=O, P–C, and P–O bonds indicates that the sodium storage active sites are reversible (Fig. S19). The reversible changes observed in these chemical bonds are confirmed to validate the sodium storage contribution from P–O–C bonds predicted by theoretical calculations. Combined with the pseudocapacitive sodium storage kinetics demonstrated in the CV curves, the sodium storage mechanism of PCT-800 can be attributed to an adsorption-based process.

Two dominant peaks were observed in the in situ Raman analysis (Fig. 5d–f). During sodiation, a broadening and attenuation of the D-band intensity was observed upon adjusting the potential from the open-circuit voltage (OCV) to 0.01 V. This spectral change is attributed to the adsorption of Na$^+$ ions at defects and pore surfaces. This adsorption process inhibits the breathing vibrations of carbon rings located at defect sites and edges. Meanwhile, the position of the D peak is blue-shifted from 1369 cm^{-1} to 1381 cm^{-1}, which clearly indicates that the phonon scattering induced by defects (such as sp^3 hybridization, edges, vacancies, doping, and so on) is weakened. Meanwhile, the position of the G peak remains stable near 1627 cm^{-1}, which is attributed to the reduction of the localized defects or the sodium storage sites of the functional groups. In addition, the possibility of significant G-band shifts resulting from Na$^+$ intercalation between carbon layers was ruled out. The gradual decrease of I_D/I_G and the strengthening of the G peak during the discharge process (Fig. 5e) are attributed to the adsorption of Na$^+$ ions at the defect sites, which leads to the reduction of the defect sites in the SC and the decrease of the electron cloud density between the graphitic carbon interlayers. The I_D/I_G value gradually increases during de-sodiation, and these trends are opposite to those of sodiation and are highly reversible. Considering the mesopore-dominated pore structure of PCT-800, the possibility of a pore-filling mechanism involving closed pores was further excluded based on the instability observed in the I_D/I_G ratio. Upon careful examination of the in situ Raman spectra, it was observed that the G-band position experiences a slight red-shift toward lower wavenumbers in Fig. 5e when the PCT-800 anode is discharged from 0.1 V to 0.01 V. Subsequently, the G-band position was observed to undergo a slight blue-shift toward higher wavenumbers in Fig. 5f, followed by a return to its original position at 0.1 V (sodiation), during charging from 0.01 V to 0.1 V. This reversible and minor shift is attributed to reversible adsorption/desorption processes occurring within the interlayer spaces of graphite crystallites at closed pore sites. The subtle alterations in electron density distribution and C–C bond lengths are induced by these processes.

As presented in Fig. 5g, the in situ XRD results show that the amorphous carbon peaks on the (002) crystal surface are not significantly shifted during sodiation and de-sodiation, which
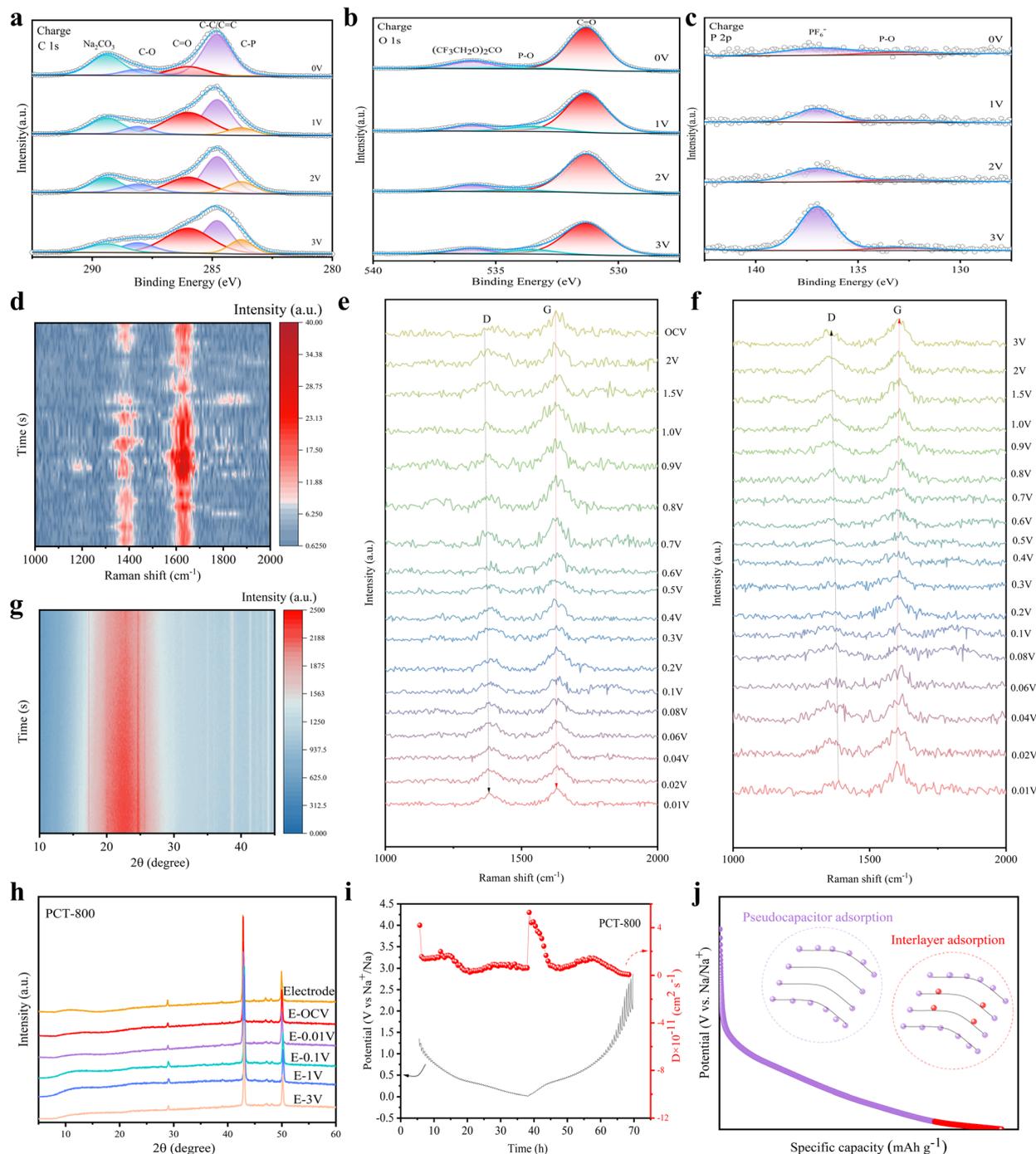
Fig. 5 PCT-800 anode (a–c) C 1s, O 1s, and P 2p spectra at different voltages during charging; (d–f) *in situ* Raman patterns for the first charging and discharging process of PCT-800; (g) *in situ* XRD patterns; (h) *ex situ* XRD patterns; (i) GITT curves; (j) sodium storage mechanism.

demonstrates that Na$^+$ ions are not inserted in large quantities into the carbon layer and the dominating sodium storage mechanism does not include an intercalation mechanism. The unshifted diffraction peaks of the electrode sheets at different voltages in the *ex situ* XRD results (Fig. 5h) likewise proved the absence of an intercalation mechanism for the dominating sodium storage process.

The kinetic properties of sodium ions were further determined by the galvanostatic intermittent titration technique (GITT) test (Fig. 5i and S19). According to Fick's second law, D_{Na^+} is calculated from the following equation:

$$D_{Na^+}\frac{4}{\pi\tau}\left(\frac{m_b V_m}{M_b S}\right)^2\left(\frac{\Delta E_s}{\Delta E_\tau}\right)^2, \qquad (4)$$

where τ is the relaxation time, m_b is the mass of the active substance, M_b is the molar mass of the active substance, V_m is the molar volume of soft carbon, S is the surface area of the active substance, and ΔE_S and ΔE_τ can be obtained from the GITT curve.

According to the CV curves, the kinetic behavior is dominated by capacitance-controlled processes with diffusion control taking a secondary position. According to the GITT curves, D_{Na^+} is approximately equal to 1×10^{-11} cm^2 s^{-1} from 1 V to 0.01 V during sodiation and the variation is not significant, indicating that hardly any Na$^+$ ions are inserted in the carbon layer. A rapid drop in the 0.01–0.5 V region occurs during the charging process, attributed to the difference in Na$^+$ concentration, which then remains essentially unchanged. Meanwhile, the diffusion coefficient increases and then decreases at about 0.51 V, which can be attributed to the formation of the SEI layer. After that, the diffusion coefficient increases and then decreases in a typical way due to the adsorption process of Na$^+$ ions at the electrode. The diffusion coefficient did not increase within the potential range of 0.05 to 0 V, indicating the absence of a typical pore-filling process.[22]

Based on comprehensive analyses of the CV and GITT curves, as well as the *in situ* XRD, *in situ* Raman, *ex situ* XRD and *ex situ* XPS results, the sodium storage mechanism can be depicted as a pseudocapacitance-dominated adsorption mechanism, as shown in the schematic diagram of Fig. 5j, which includes the adsorption of Na$^+$ ions on surfaces, defects, functional groups, or interlayer active sites. This sodium storage mechanism exhibits exceptionally rapid kinetics, which facilitates high-rate charge/discharge processes. Consequently, the charging duration is significantly reduced.

Electrochemical characterization of button capacitor devices and PCs

Given the excellent electrochemical behavior of the prepared SCs, great potential has been shown for commercial applications. Herein, so as to further evaluate the practical performance, a button capacitor PCT-800‖NFPP with PCT-800 anode and NFPP cathode (Fig. S20) was fabricated. Meanwhile, a button full cell CHC‖NFPP with commercial hard carbon (CHC) anode and NFPP cathode was also fabricated for comparison. The GCD curve of the capacitor was observed to be similar to the half-cell curve of the cathode NFPP with two plateaus (Fig. S21), and the higher plateau capacity implies a higher energy storage capacity.

The CV curves of CHC‖NFPP (Fig. 6a) and PCT-800‖NFPP (Fig. 6b) show reversible redox reactions, and the broad peaks observed for PCT-800‖NFPP is attributed to the high density of defects present on the surface of the PCT-800 anode. The b values (Fig. S22) were also calculated to analyze the contribution of the capacitance-controlled and diffusion-controlled processes, and the higher b value of the PCT-800 material compared with that of CHC suggests a greater contribution of pseudocapacitance and superior rate capability at high currents.

The assembled SICs deliver ultrahigh capacities of 76.54 mA h g^{-1} and 70.73 mA h g^{-1} at 0.05 A g^{-1} and 1 A g^{-1}

(Fig. 6c), respectively, which reflects the excellent rate capability of the PCT-800 anode. The cycling performance of the SIC (Fig. 6g) demonstrated a maximum capacity of 71.23 mA h g^{-1} (based on the sum of the active substance masses of the cathode and anode) at 1 A g^{-1} (15C), with a capacity retention rate of 95.65% after 500 cycles. The excellent rate capability and cycling performance indicate that the practical soft carbon anode PCT-800 has great potential for commercialization in high-power-density SICs.

The energy density and power density are calculated comparing the SIC with or without PCT-800 pre-sodiation (Fig. 6d–e). The results show that at a power density of 140 W kg^{-1}, the energy density of the pre-sodiation capacitor is 216.37 Wh kg^{-1} (based on the total mass of active material in the cathode and anode), which is much higher than that of the capacitor without pre-sodiation (45.16 Wh kg^{-1}). It is worth mentioning that the power density of 2891.90 W kg^{-1} is accompanied by a high energy density of 196.81 Wh kg^{-1} at a high current density of 1 A g^{-1} (Fig. S23). When converted to volumetric energy density, a volumetric energy density of 248.39 Wh L^{-1} is achieved at a volumetric power density of 3649.87 W L^{-1}. An ultrahigh volumetric energy density of 273.08 Wh L^{-1} is achieved at a volumetric power density of 180 W L^{-1}, significantly surpassing those of commercially available SICs (typically ≤160 Wh L^{-1}).

The evaluation was scaled up from button capacitors to PCs to assess commercial viability (Fig. S24–S26). For the single-layer PC (Fig. 6h–i), a specific capacity of 45 mA h g^{-1} was measured at a current density of 0.1 A g^{-1}. A capacity retention rate of 99.58% was maintained after 70 cycles, indicating exceptional cycling stability. Under these conditions, an energy density of 174.21 Wh kg^{-1} was achieved at a power density of 255.25 W kg^{-1}. Notably, superior rate capability was demonstrated. 57% of the capacity measured at a C-rate of 1C was retained at the higher rate of 20C.

To evaluate commercial potential, the performances of CHC and PCT-800 were comprehensively compared in Fig. 6f. Commercial viability of PCT-800 was assessed across six metrics: ICE, energy density, rate capability, volumetric specific capacity, safety, and tap density. At a power density of approximately 2500 W kg^{-1}, the energy density of PCT-800 (196.81 Wh kg^{-1}) is measured to be 59.13% higher than that of CHC (123.68 Wh kg^{-1}). Although only a marginal difference in ICE is observed between PCT-800 (77.60%) and CHC (75.10%), a significantly superior rate capability and volumetric specific capacity are exhibited by PCT-800. At 2 A g^{-1}, the specific capacity of PCT-800 (181.76 mA h g^{-1}) is enhanced by 217.82% compared to CHC (57.19 mA h g^{-1}). This improvement is further amplified when considering the 55.56% higher tap density of PCT-800 (1.26 g cm^{-3}) *versus* CHC (0.81 g cm^{-3}). Consequently, at 0.1 A g^{-1}, the volumetric specific capacity of PCT-800 (306.58 mA h cm^{-3}) is elevated by 46.33% relative to CHC (209.51 mA h cm^{-3}). Safety performance, a critical parameter for fast-charging batteries, was evaluated in Fig. S27. After high-rate charge/discharge cycling at 30C, sodium dendrites are visibly observed on the CHC anode, whereas no dendrite formation is detected on the PCT-800 anode. This
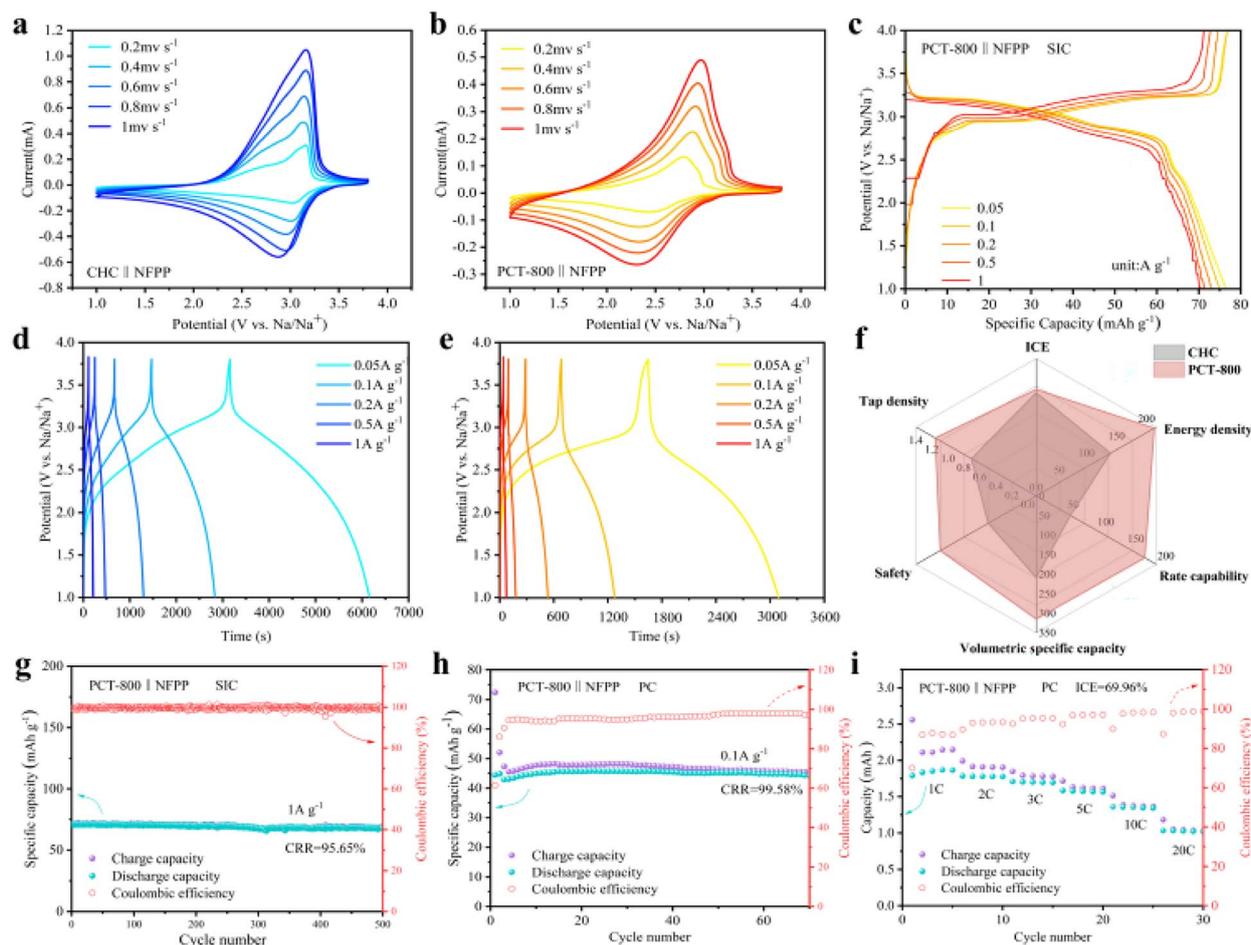
Fig. 6 (a and b) CV curves of CHC‖NFPP and PCT-800‖NFPP; (c) rate capability of the PCT-800 SIC; (d) V–t curves of SIC with pre-sodiation; (e) V–t curves of SIC without pre-sodiation; (f) comprehensive comparison of the performance of CHC and PCT-800; (g) cycling performance of the PCT-800 SIC; (h) cycling performance of the PCT-800 PC; (i) rate capability of the PCT-800 PC.

dendrite suppression capability and enhanced safety of PCT-800 are confirmed to align with theoretical predictions, validating its exceptional reliability for practical applications.

Conclusions

In summary, SC with a high tap density (1.26 g cm^{-3}) and carbon yield (80%) was synthesized through *in situ* phosphorus crosslinking strategies. Combined with *ex/in situ* characterization and theoretical calculations, PCT-800 was demonstrated to exhibit substantial reversible adsorption at surface/defect/functional group sites, complemented by minimal adsorption at interlayer active sites. The surface modification *via* P–O–C bonds was found to regulate electron distribution, reduce nucleation barriers, and induce uniform nucleation, thereby suppressing initial dendrite formation at its origin. Furthermore, the slope-dominated sodium storage mechanism indicates exceptionally rapid kinetics in PCT-800, with electrode potentials significantly higher than the sodium metal deposition potential. This reveals the fundamental origin of fast-charging capability and enhanced safety in

phosphorus-doped SCs. Comprehensive structural characterization and mechanistic investigation in this work provide clear insights into the correlations between SC microstructures and their corresponding rate capability and sodium storage behavior. Specifically, the as-prepared PCT-800 delivered a high capacitive capacity of 308 mA h g^{-1} at 0.03 A g^{-1} and an outstanding rate capability (181 mA h g^{-1} at 1 A g^{-1}), with an ICE of 77.6%. When assembled with NFPP into a SIC, an exceptionally high capacity of $71.23 \text{ mA h g}^{-1}$ was achieved at 1 A g^{-1}, with 95.65% capacity retention rate after 500 cycles. An ultrahigh energy density of $196.81 \text{ Wh kg}^{-1}$ was achieved at $2891.90 \text{ W kg}^{-1}$, greatly surpassing previous reports ($<120 \text{ Wh kg}^{-1}$). In a PC configuration, a high energy density of 56.04 Wh kg^{-1} can be achieved at a high rate of 20C, with full charge accomplished within 96 seconds. More importantly, practical applicability was successfully shown by the PCs, which exhibited rapid sodium storage behavior and high safety. It should be emphasized that this work paves the way for future commercialization of SCs and the development of SICs with both ultrahigh energy and power densities.

Author contributions

Bo Xiong: writing – original draft, methodology, investigation, formal analysis, data curation, conceptualization. Jieming Cai: methodology. Biao Zhong: software. Luoming Zhang: resources. Dongxiao Li: data curation. Jie Li: data curation. Juan Tian: resources. Xiongwei Luo: resources. Fei Yao: resources. Zhiyu Zeng: resources. Wentao Deng: funding acquisition. Hongshuai Hou: supervision, funding acquisition. Jialuo She: validation, visualization. Tianyun Qiu: writing – review & editing. Guoqiang Zou: investigation, resources, writing – review & editing. Dulin Yin: project administration. Xiaobo Ji: funding acquisition.

Conflicts of interest

The authors declare that they have no known competing financial interests or personal relationships that could have appeared to influence the work reported in this paper.

Data availability

The data that support the findings of this study are available in the supplementary information (SI) of this article. Supplementary information: materials synthesis, materials characterizations, electrochemical measurements, theoretical calculations, Fig. S1–S27, Tables S1–S5 and references. See DOI: https://doi.org/10.1039/d5sc07164j.

Acknowledgements

Notes and references

1 S. Tao, Z. Cao, X. Xiao, Z. Song, D. Xiong, Y. Tian, W. Deng, Y. Liu, H. Hou and G. Zou, Tunable Platform Capacity of Metal–Organic Frameworks via High-Entropy Strategy for Ultra-Fast Sodium Storage, *Nano-Micro Lett.*, 2025, **17**, 201.

2 H. Hao, R. Tan, C. Ye and C. T. J. Low, Carbon-coated current collectors in lithium-ion batteries and supercapacitors: Materials, manufacture and applications, *Carbon Energy*, 2024, **6**, e604.

3 W. Li, Q. A. Huang, Y. Bai, J. Wang, L. Wang, Y. Liu, Y. Zhao, X. Li and J. Zhang, Model reduction of fractional impedance spectra for time–frequency analysis of batteries, fuel cells, and supercapacitors, *Carbon Energy*, 2024, **6**, e360.

4 Z. Xu, Y. Yuan, Q. Tang, X. Nie, J. Li, Q. Sun, N. Ci, Z. Xi, G. Han and L. Ci, Facile construction of a multilayered interface for a durable lithium-rich cathode, *Carbon Energy*, 2023, **5**, e332.

5 H. Xiao, X. Li and Y. Fu, Advances in anion chemistry in the electrolyte design for better lithium batteries, *Nano-Micro Lett.*, 2025, **17**, 149.

6 N. Hong, J. Li, H. Wang, X. Hu, B. Zhao, F. Hua, Y. Mei, J. Huang, B. Zhang, W. Jian, J. Gao, Y. Tian, X. Shi, W. Deng, G. Zou, H. Hou, Z. Hu, Z. Long and X. Ji, Regulating Phase Transition and Restraining Fe Distortion at High Potential Window via Rare Earth Metal Incorporation on O3-Type Layered Cathodes, *Adv. Funct. Mater.*, 2024, **34**, 2402398.

7 P. Cai, K. Zou, X. Deng, B. Wang, M. Zheng, L. Li, H. Hou, G. Zou and X. Ji, Comprehensive understanding of sodium-ion capacitors: definition, mechanisms, configurations, materials, key technologies, and future developments, *Adv. Energy Mater.*, 2021, **11**, 2003804.

8 N. Hong, S. Zhang, J. Li, H. Wang, J. Huang, X. Hu, B. Zhang, F. Hua, J. Zeng, W. Jian, C. Sun, N. Bugday, W. Deng, G. Zou, H. Hou, Z. Hu, Z. Long, Y. Wu and X. Ji, Full-Scale Regulation Enabled High-Performance Sodium O3-Type Layered Cathodes, *Angew. Chem., Int. Ed.*, 2025, **64**, e202423479.

9 X. Xiao, S. Tao, H. Lian, Y. Tian, W. Deng, H. Hou, G. Zou and X. Ji, Unveiling the Microscopic Origin of Ultrahigh Initial Coulombic Efficiency of High-Entropy Metal–Organic Frameworks for Sodium Storage, *ACS Nano*, 2024, **18**, 28444–28455.

10 Y. Huang, X. Zhong, X. Hu, Y. Li, K. Wang, H. Tu, W. Deng, G. Zou, H. Hou and X. Ji, Rationally Designing Closed Pore Structure by Carbon Dots to Evoke Sodium Storage Sites of Hard Carbon in Low-Potential Region, *Adv. Funct. Mater.*, 2024, **34**, 2308392.

11 Y. Huang, X. Hu, Y. Li, X. Zhong, Z. He, Z. Geng, S. Gan, W. Deng, G. Zou, H. Hou and X. Ji, Demystifying the Influence of Precursor Structure on S-Doped Hard Carbon Anode: Taking Glucose, Carbon Dots, and Carbon Fibers as Examples, *Adv. Funct. Mater.*, 2024, **34**, 2403648.

12 C. Wu, Y. Yang, Y. Zhang, H. Xu, W. Huang, X. He, Q. Chen, H. Dong, L. Li, X. Wu and S. Chou, Industrial-Scale Hard Carbon Designed to Regulate Electrochemical Polarization for Fast Sodium Storage, *Angew. Chem., Int. Ed.*, 2024, **63**, e202406889.

13 X.-Y. Wang, K.-Y. Zhang, M.-Y. Su, H.-H. Liu, Z.-Y. Gu, D. Dai, B. Li, J.-W. Wang, X.-Y. He and X.-L. Wu, Coal-derived flaky hard carbon with fast Na$^+$ transport kinetic as advanced anode material for sodium-ion batteries, *Carbon*, 2024, **229**, 119526.

14 Y. Qi, Y. Lu, F. Ding, Q. Zhang, H. Li, X. Huang, L. Chen and Y. S. Hu, Slope-Dominated Carbon Anode with High Specific Capacity and Superior Rate Capability for High Safety Na-Ion Batteries, *Angew. Chem., Int. Ed.*, 2019, **58**, 4361–4365.

15 L. Ji, Y. Zhao, L. Cao, Y. Li, C. Ma, X. Qi and Z. Shao, A fundamental understanding of structure evolution in the synthesis of hard carbon from coal tar pitch for high-performance sodium storage, *J. Mater. Chem. A*, 2023, **11**, 26727–26741.

16 J. Liu, Y. You, L. Huang, Q. Zheng, Z. Sun, K. Fang, L. Sha, M. Liu, X. Zhan, J. Zhao, Y. C. Han, Q. Zhang, Y. Chen, S. Wu and L. Zhang, Precisely Tunable Instantaneous

Carbon Rearrangement Enables Low-Working-Potential Hard Carbon Toward Sodium-Ion Batteries with Enhanced Energy Density, *Adv. Mater.*, 2024, **36**, 2407369.

17 S. Xiao, Y. J. Guo, H. X. Chen, H. Liu, Z. Q. Lei, L. B. Huang, R. X. Jin, X. C. Su, Q. Zhang and Y. G. Guo, Insight into the Role of Closed-Pore Size on Rate Capability of Hard Carbon for Fast-Charging Sodium-Ion Batteries, *Adv. Mater.*, 2025, **37**, 2501434.

18 J. Yan, H. Li, K. Wang, Q. Jin, C. Lai, R. Wang, S. Cao, J. Han, Z. Zhang, J. Su and K. Jiang, Ultrahigh Phosphorus Doping of Carbon for High-Rate Sodium Ion Batteries Anode, *Adv. Energy Mater.*, 2021, **11**, 2003911.

19 L. Yuan, Q. Zhang, Y. Pu, X. Qiu, C. Liu and H. Wu, Modulating Intrinsic Defect Structure of Fibrous Hard Carbon for Super-Fast and High-Areal Sodium Energy Storage, *Adv. Energy Mater.*, 2024, **14**, 2400125.

20 Y. Yang, C. Wu, X. X. He, J. Zhao, Z. Yang, L. Li, X. Wu, L. Li and S. L. Chou, Boosting the Development of Hard Carbon for Sodium-Ion Batteries: Strategies to Optimize the Initial Coulombic Efficiency, *Adv. Funct. Mater.*, 2023, **34**, 2302277.

21 Y. Li, Y. Yuan, Y. Bai, Y. Liu, Z. Wang, L. Li, F. Wu, K. Amine, C. Wu and J. Lu, Insights into the Na$^+$ Storage Mechanism of Phosphorus-Functionalized Hard Carbon as Ultrahigh Capacity Anodes, *Adv. Energy Mater.*, 2018, **8**, 1702781.

22 H. He, J. He, H. Yu, L. Zeng, D. Luo and C. Zhang, Dual-Interfering Chemistry for Soft-Hard Carbon Translation toward Fast and Durable Sodium Storage, *Adv. Energy Mater.*, 2023, **13**, 230035.